



Composites of Carbon Nanofibers and Nanophase Pt-SnO₂ for Lithium-Ion Batteries

Geon-Hyoung An,^a Si-Jin Kim,^b Kyung-Won Park,^b and Hyo-Jin Ahn^{a,z}

^aDepartment of Materials Science and Engineering, Seoul National University of Science and Technology, Seoul 139-743, Korea

^bDepartment of Chemical and Environment Engineering, Soongsil University, Seoul 156-743, Korea

Composites of carbon nanofibers (CNFs) and nanophase Pt-SnO₂ were synthesized using electrospinning followed by carbonization, for use as anode materials in Lithium-ion batteries (LIBs). Composites of CNFs and nanophase Pt-SnO₂ (sample B) exhibit the highest capacity (~621.9 mAh/g at the 50th cycle) and excellent cyclic stability as compared to conventional CNFs and composites of CNFs and nanophase SnO₂ (sample A). The result indicates that the improvement in performance of CNFs by the incorporation of nanophase Pt-SnO₂ can be explained by the enhancement in electrical conductivity and the increase in the number of electrochemical active sites.

© 2014 The Electrochemical Society. [DOI: 10.1149/2.009403ssl] All rights reserved.

Manuscript submitted December 13, 2013; revised manuscript received January 7, 2014. Published January 14, 2014.

High-performance lithium-ion batteries (LIBs) have recently attracted considerable attention as devices for efficient energy storage due to their high energy density, high operating voltage, high cycling stability, and low self-discharge rate, which are advantageous for various applications (i.e., mobile phones, laptops, electrical vehicles, and robotics).¹⁻⁴ LIBs consist of four main components: the anode, cathode, electrolyte, and separator. Anode materials that are currently under consideration include carbon-based materials (graphite, carbon nanotubes (CNTs), and carbon nanofibers (CNFs)), lithium alloys (LiSi, LiAl, and LiSn), 3D-metal oxides (SnO₂, Co₃O₄, Fe₂O₃, and MnO₂), nitrides (Sb₃N, SiN, and TiN), and Si/Sn-based materials (Si, Sn, SiTi, SnCo, and SnNi).⁵ Among these, carbon-based materials show the most potential for use as LIB anodes because of their low cost and high cycling performance.⁶ In particular, CNFs provide advantages of low cost, good electrical conductivity (10⁵ S/cm), large surface area (462 m²/g), and good thermal/chemical stability.⁷ However, the use of CNFs as LIB anodes is limited by their low theoretical discharge capacity of 372 mAh/g.⁸ There have been attempts to overcome this problem by incorporating metal oxides (M_xO_y, M = Sn, Co, Ti, and Mn) into CNFs to increase their high specific capacity and cycling performance compared to conventional CNFs. For example, Lin et al. demonstrated that MnO_x-embedded CNF composites synthesized using electrospinning showed a discharge capacity of 444 mAh/g at the 50th cycle; the current density was 50 mA/g during the 50th cycle, showing high cycle performance.⁹ However, to the best of our knowledge, research on CNF composites simultaneously containing nanophase metals and metal oxides for high performance LIBs has not been previously reported.

In this study, we synthesized composites of CNFs and nanophase Pt-SnO₂ and investigated their electrochemical properties, including capacity and cyclic stability, to determine their suitability as candidates for high-performance LIB anode materials. Our results indicate that the nanophase Pt-SnO₂ embedded within the CNFs plays an important role in improving the specific capacity and cyclic stability of the composite.

Experimental

Composites of CNFs and nanophase Pt-SnO₂ were prepared by electrospinning followed by carbonization. CNFs containing nanophase SnO₂ were first synthesized by dissolving polyacrylonitrile (PAN, M_w = 150,000 g/mol, Aldrich), polyvinylpyrrolidone (PVP, M_w = 1,300,000 g/mol, Aldrich), and tin(II) chloride dihydrate (SnCl₂ · 2H₂O, Aldrich) in N,N-Dimethylformamide (DMF, Aldrich). To fabricate composites of CNFs and nanophase Pt-SnO₂, chloroplatinic acid hydrate (H₂PtCl₆ · xH₂O, Aldrich) was then added to the above-mentioned mixture at an 8:2 mole ratio of Sn to Pt precursors.

The as-prepared samples for stabilization were heat-treated at 280°C for 5 h in ambient air, and then carbonization was achieved by heating the sample up to 800°C in N₂ gas (99.999%) and incubating it for 2 h. In addition, for comparison, the same method was used to synthesize conventional CNFs from PAN and PVP precursors dissolved in DMF without the tin(II) chloride dehydrate and chloroplatinic acid hydrate. We thus prepared three different types of electrode materials: conventional CNFs, composites of CNFs and nanophase SnO₂, and composites of CNFs and nanophase Pt-SnO₂ (herein referred to as conventional CNFs, sample A, and sample B, respectively).

The morphological properties of the electrodes were analyzed by field emission scanning electron microscopy (FESEM; Hitachi S-4800) and multi-functional transmission electron microscopy (MULTI/TEM; Tecnai G², KBSI Gwangju Center) with energy dispersive X-ray spectroscopy (EDS; Thermo NORAN system 7). The crystallinity of the electrodes was measured by X-ray diffraction (XRD; Rigaku D/Max 2500 V).

The Li-ion insertion/extraction behavior of the samples was examined using Li coin cells (CR2032, Hohsen Corporation). The coin cells were assembled in an Ar-filled glove box (<5 ppm, H₂O and O₂). The electrochemical properties of all samples were measured at a current density of 0.1 C (29 mA/g) in a voltage range of 0.0–2.0 V using a WMPG 3000 battery cycler system. To examine the electrical properties of the electrodes, electrochemical impedance spectra (EIS) were obtained by measuring the impedance at a voltage of 5 mV over an AC frequency range of 10 mHz to 100 kHz.

Results and Discussion

Figures 1a–1c show FESEM images for conventional CNFs, sample A, and sample B. All samples exhibit smooth surfaces and uniform morphologies. In particular, samples A and B exhibit the formation of uniform nanofibers without any beads or agglomerated SnO₂ or Pt-SnO₂ on the surface, implying that these materials were uniformly embedded within the CNFs. The average diameters of CNFs are estimated to be about 215–248 nm for the conventional CNFs, 184–201 nm for sample A, and 198–219 nm for sample B. Samples A and B are smaller in diameter compared to conventional CNF electrodes. The reason is because carbon is slightly consumed during the formation of CNFs owing to a partial oxidation–reduction reaction between the Sn precursor and PVP.¹⁰ In addition, the diameter of sample B is slightly larger than that of sample A owing to the addition of Pt. Figure 1d shows a schematic of sample B, indicating the three different phases that comprise the electrode, namely the CNFs and the well-distributed nanophase Pt and SnO₂ within them.

Figure 2 shows low-resolution TEM images (a–c) and high-resolution TEM images (d–f) of the conventional CNFs, sample A, and sample B. The conventional CNFs, shown in Figures 2a and 2d, exhibit a uniform level of contrast over the whole sample image, indicating

^zE-mail: hjahn@seoultech.ac.kr

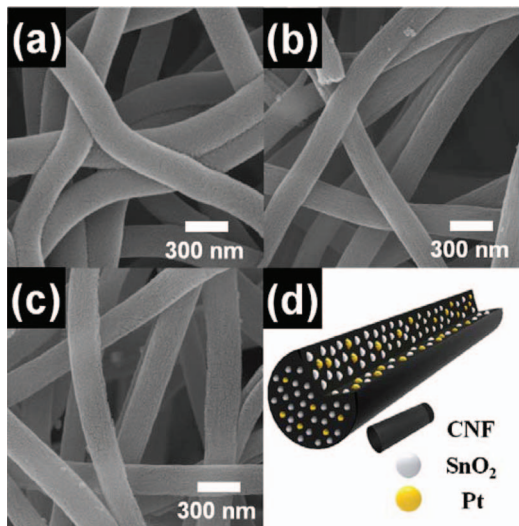


Figure 1. SEM images obtained from (a) conventional CNFs, (b) sample A, and (c) sample B. (d) A schematic of composites of CNFs and nanophase Pt-SnO₂.

that these samples consist of only one phase. However, in the case of sample A (Figures 2b and 2e), the composite electrodes exhibit dark nanospheres that can be attributed to the SnO₂ nanophase, and bright regions that can be attributed to the CNFs. Furthermore, it is noted that the nanophase SnO₂ domains in sample A (Figure 2e) range from 8–11 nm in size and exhibit some agglomeration (Figure 2b). Interestingly, as shown in Figures 2c and 2f, the introduction of nanophase Pt in SnO₂-CNF electrodes decreases the size of the nanophase SnO₂ and increases the distribution of the nanophases embedded within the CNFs. That is, the addition of the nanophase Pt plays an important role in preventing the agglomeration of the nanophase SnO₂ in the CNFs.¹¹ This was confirmed using the selected-area electron diffraction (SAED) patterns shown in the insets of Figure 2a–2c. The SAED patterns of the conventional CNFs exhibit a broad diffuse ring around the (000) spot, implying that these samples are amorphous. The SAED patterns of sample A exhibit a broad diffuse ring with outstanding spots, implying the successful formation of polycrystalline SnO₂ in the amorphous CNFs. However, sample B presents sharp ring patterns with a broad diffuse ring around the (000) spot, indicating good distribution of small-sized Pt and SnO₂. Both the size and the distribution of the nanophase Pt-SnO₂ domains embedded within the CNFs can influence this material's electrochemical performance in

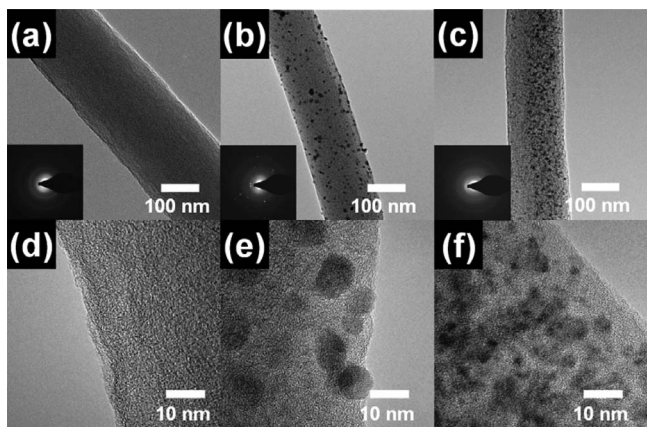


Figure 2. [(a)–(c)] Low-resolution TEM images with selected area electron diffraction patterns (SAED) and [(d)–(f)] high-resolution TEM images obtained from (a) conventional CNFs, (b) sample A, and (c) sample B.

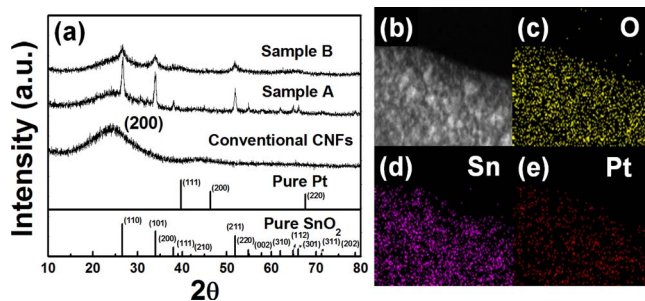


Figure 3. (a) XRD patterns obtained from conventional CNFs, sample A, and sample B. [(b)–(e)] TEM-EDS mapping data obtained from sample B.

LIBs owing to the effects of these factors on electrical conductivity and the number of electrochemical active sites.

Figure 3a shows XRD patterns corresponding to conventional CNFs, sample A, and sample B. The conventional CNFs, exhibit only a broad peak around 25°, corresponding to the (002) layers of the graphite. The characteristic peaks of sample A are observed at $2\theta = 26.5^\circ, 33.9^\circ, 37.9^\circ$ and 51.7° , corresponding to the (110), (101), (200), and (211) planes. They were indexed as the crystalline SnO₂ phase having the tetragonal rutile structure (space group P4₂/mmn [136]) (JCPDS card No. 71–0652). Sample B also exhibits the same characteristic peaks as sample A. However, sample B shows broader characteristic peaks with low diffracted intensity. That is, the width of the diffraction curve for sample B increases as the size of the nanophase SnO₂ domains decreases. This can be explained by using the Scherrer formula to calculate the size of the nanophase SnO₂ domains, as follows:

$$D = 0.9\lambda / (\beta \cos \theta) \quad [1]$$

where λ , β , and θ are the X-ray wavelength, the full width at half maximum (FWHM), and the Bragg angle. The particle size is in inverse proportion to the FWHM. The width of the diffraction curve of sample B is larger than that of sample A. Thus, using the above-mentioned equation with the (110), (101), and (211) planes, the sizes of the nanophase SnO₂ in the CNFs are obtained as 13.0 nm for sample A and 4.5 nm for sample B, which is in good agreement with the TEM results. In addition, no characteristic peaks of nanophase Pt in sample B are observed because only a small amount of the Pt precursor is added. Therefore, to examine the existence of the nanophase Pt, TEM-EDS mapping, as shown in Figures 3b–3e, was performed for sample B after calcination. The result confirmed that Sn (purple dots) and Pt atoms (red dots) are uniformly dispersed in the CNF matrix. Thus, these results indicate that the composites of CNFs and nanophase Pt-SnO₂ were successfully synthesized using an electrospinning method.

Figure 4a shows the typical insertion/extraction profiles at the 1st cycles for conventional CNFs, sample A, and sample B. The potential continuously decreases to 0.0 V during the first Li insertion. The specific capacities observed at the 1st cycle are ~580.0 mAh/g for conventional CNFs, ~755.3 mAh/g for sample A, and ~1106.6 mAh/g for sample B. Also, the specific capacities at the 2nd cycle decrease to ~381.5 mAh/g for conventional CNFs, ~510.4 mAh/g for sample A, and ~705.7 mAh/g for sample B. This is due to the large capacity losses between the 1st and 2nd cycle resulting from the reduction reaction of SnO₂ through the irreversible reactions given in Eq. 2.¹²



Nevertheless, sample B exhibits excellent specific capacity as compared to conventional CNFs and sample A. This can be explained by two reasons: one is related to the improved electrical conductivity of the electrode owing to the introduction of well-distributed nanophase Pt within the composite electrodes. Figure 4b shows the EIS results before the Li ion insertion/extraction performance test of conventional CNFs, sample A, and sample B. The semicircles in the medium-frequency region indicate the charge transfer impedance (R_{ct})

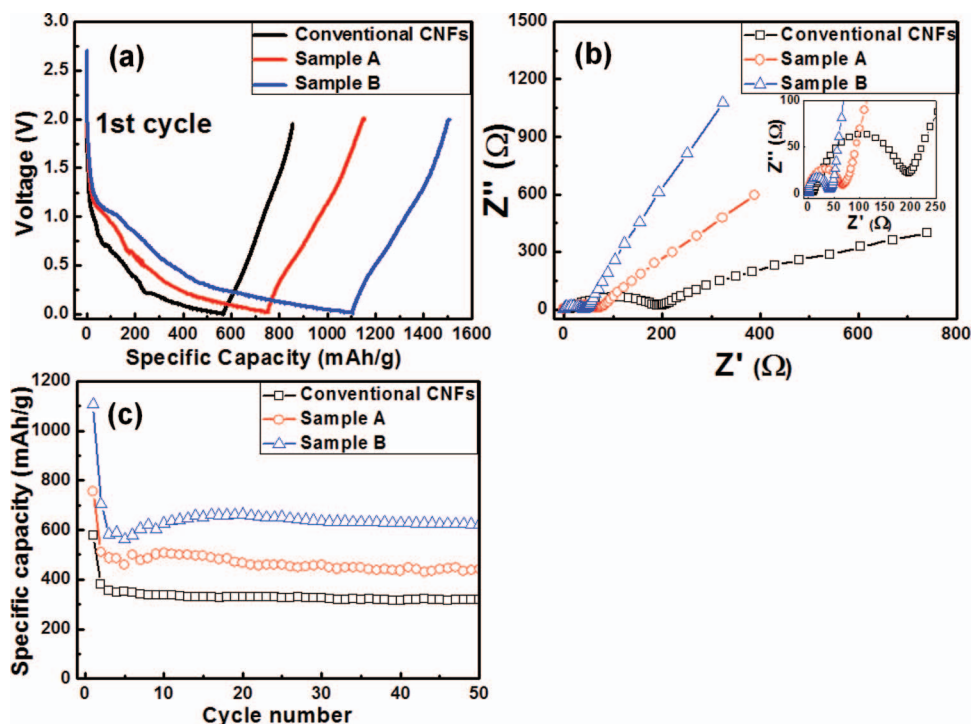


Figure 4. (a) Insertion/extraction profiles of 1st cycle of conventional CNFs, sample A, and sample B evaluated in the voltage range 0.0–2.0 V at a current rate of 0.1 C. (b) EIS data before the Li ion insertion/extraction performance test of conventional CNFs, sample A, and sample B. (c) Cycle performances of conventional CNFs, sample A, and sample B at a current rate of 0.1 C up to 50 cycles.

at the electrode/electrolyte interface, and the sloped lines indicate the Warburg impedance, which related to the diffusion of Li within the electrodes. Owing to the presence of nanophase Pt, sample B shows lower R_{ct} (41.7 Ω) than sample A (66.5 Ω) and conventional CNFs (195.9 Ω), and higher Warburg impedance. The other reason is related to the increase in the electrochemical active sites due to the size reduction of the nanophase SnO_2 . Reducing the size of the active material for LIBs improves its specific capacity. Figure 4c shows the cycle performances of conventional CNFs, sample A, and sample B at a current rate of 0.1 C up to 50 cycles. After the 50th cycle, the reversible specific capacities are observed to be ~ 320.5 for conventional CNFs, ~ 441.6 for sample A, and ~ 621.9 mAh/g for sample B. Thus, sample B exhibits superior reversible specific capacity compared to conventional CNFs and sample A. Furthermore, the CNF-based structures of all the samples contributed to their excellent cycle performance. In general, SnO_2 materials when used as anodes undergo a large volume change during Li insertion/extraction cycling, resulting in quick fading of their capacity. The CNF matrix prevents this large change in volume of the embedded SnO_2 . As a result, sample B exhibited the highest reversible capacity as well as excellent cyclic stability.

Conclusions

Composites of CNFs and nanophase Pt- SnO_2 (sample B) were successfully synthesized by electrospinning followed by carbonization. This sample exhibited higher reversible capacity (~ 621.9 mAh/g at the 50th cycle) compared to conventional CNFs and those containing only

nanophase SnO_2 (sample A). This improvement arises from the synergic effect of the nanophase Pt and the nanophase SnO_2 to enhance the electrical conductivity and increase the number of electrochemically active sites. Therefore, composites of CNFs and nanophase Pt- SnO_2 show promise as alternative anode materials for high-performance LIBs.

Acknowledgment

This research was supported by Basic Science Research Program through the National Research Foundation of Korea (NRF) funded by the Ministry of Education, Science and Technology (2012–007444).

References

1. J.-S. Bridel, T. Azais, M. Morcrette, J.-M. Tarascon, and D. Larcher, *Chem. Mater.*, **22**, 1229 (2010).
2. M. Wu, J. Chen, C. Wang, F. Wang, and B. Yi, *Electrochimica Acta*, **105**, 462 (2013).
3. R. Yang, Z. Wang, J. Liu, and L. Chen, *Electrochem. Solid-State Lett.*, **7**, A496 (2004).
4. Q. Si, K. Hanai, T. Ichikawa, A. Hirano, N. Imanishi, O. Yamamoto, and Y. Takeda, *J. Power Sources*, **196**, 6982 (2011).
5. F. Cheng, J. Liang, Z. Tao, and J. Chen, *Adv. Mater.*, **23**, 1695 (2011).
6. G.-H. An and H.-J. Ahn, *Electrochem. Solid-State Lett.*, **2**, M33 (2013).
7. G.-H. An and H.-J. Ahn, *Carbon*, **65**, 87 (2013).
8. B. Simon, S. Flandrois, K. Guerin, A. Fevrier-Bouvier, I. Teulat, and P. Biensan, *J. Power Sources*, **81**, 312 (1999).
9. Z. Lin, L. Ji, M. D. Woodroof, and X. Zhang, *J. Power Sources*, **195**, 5025 (1999).
10. Z. Yang, G. Du, Z. Guo, X. Yu, S. Li, Z. Chen, P. Zhang, and H. Liu, *Nanoscale*, **2**, 1011 (2010).
11. M. B. Sahana, C. Sudakar, A. Dixit, J. S. Thakur, R. Naik, and V. M. Naik, *Acta Mater.*, **60**, 1072 (2012).
12. Y. Jiang, T. Yuan, W. Sun, and M. Yan, *Appl. Mater. Interfaces*, **4**, 6216 (2012).